inorganics

MDPI

Communication

$NiCo(OH)_2/NiCo_2O_4$ as a Heterogeneous Catalyst for the Electrooxidation of 5-Hydroxymethylfurfural

Wen Li, Di Yin, Wanxin Liu, Yi Li and Yijin Wu *

Hunan Engineering Research Center for Monitoring and Treatment of Heavy Metals Pollution in the Upper Reaches of XiangJiang River, Key Laboratory of Functional Metal-Organic Compounds of Hunan Province, College of Chemistry and Material Science, Hengyang Normal University, Hengyang 421001, China; wenliw2025@126.com (W.L.); z3102685535@163.com (D.Y.); 13875879102@163.com (W.L.); liyi12345678901@foxmail.com (Y.L.)

* Correspondence: wuyj313978@163.com or yjwu@hynu.edu.cn

Abstract

The electrochemical oxidation of biomass-derived 5-hydroxymethylfurfural (HMF) coupled with water electrolysis for green hydrogen production is a promising strategy to address energy crises and environmental pollution. Despite the suitable adsorption energy for HMF due to their partially filled d-band electronic structures, Ni- or Co-based oxides/hydroxides still face challenges in insufficient activity and stability. In this study, a porous heterogeneous nickel cobalt oxide/hydroxide growth on nickel foam (NF), which is defined as NF@NiCo-H/O, was developed via immersion in concentrated alkali solution. Compared with the single-component NiCo oxides, the NF@NiCo-H/O catalyst exhibits a lower application potential of only 1.317 V, 1.395 V, and 1.443 V to achieve current densities of 20, 50, and 100 mA cm^{-2}, respectively, in an alkaline solution containing HMF. Additionally, it demonstrates rapid reaction kinetics with a Tafel slope of 27.6 mV dec^{-1} and excellent cycling stability. Importantly, the presence of more high-valent Ni^{3+}-O species on the catalyst surface contributes to its exceptional selectivity for 2,5-furandicarboxylic acid (86.7%), Faradaic efficiency (93.1%), and conversion rate (94.4%). This catalyst provides some theoretical guidance for the development of biomass electrooxidation catalysts for sustainable energy and chemical production.

Keywords: 5-hydroxymethylfurfural; heterogeneous catalyst; nickel–cobalt compounds; electrochemical performance; active species

check for updates

Academic Editor: Axel Klein

Received: 21 April 2025
Revised: 13 June 2025
Accepted: 21 June 2025
Published: 24 June 2025

Citation: Li, W.; Yin, D.; Liu, W.; Li, Y.; Wu, Y. $NiCo(OH)_2/NiCo_2O_4$ as a Heterogeneous Catalyst for the Electrooxidation of 5-Hydroxymethylfurfural. *Inorganics* **2025**, *13*, 211. https://doi.org/10.3390/inorganics13070211

Copyright: © 2025 by the authors. Licensee MDPI, Basel, Switzerland. This article is an open access article distributed under the terms and conditions of the Creative Commons Attribution (CC BY) license (https://creativecommons.org/licenses/by/4.0/).

1. Introduction

In the context of dwindling global fossil fuels and the transition to green energy, the oxidation reaction of 5-hydroxymethylfurfural (HMF) has emerged as a sustainable biomass conversion technology of significant research importance [1]. As a renewable biomass platform molecule, HMF can be oxidized to produce 2,5-furandicarboxylic acid (FDCA), a high-value chemical that serves as an alternative to traditional petrochemical feedstocks [2]. The electrochemical oxidation of HMF (HMFOR) to FDCA not only enables the efficient utilization of biomass resources but also reduces energy consumption when coupled with water electrolysis for hydrogen production [3]. Moreover, compared to traditional water electrolysis, the HMF electro-oxidation process features lower oxidation potentials and faster reaction kinetics, which enhance hydrogen production efficiency and mitigate potential safety risks [1,2]. Therefore, the in-depth investigation of the surface and interfacial structures of HMFOR catalysts, as well as their reaction mechanisms, is of

significant importance for promoting the electrochemical upgrading of biomass and the development of sustainable energy.

At present, the large-scale commercialization of electrochemical oxidation of HMF to produce FDCA faces many severe challenges. The construction of high-performance and cost-effective electrocatalysts is one of the key challenges to address the above-mentioned challenges. A variety of non-noble metal electrocatalysts, including metal oxides (oxides [4,5], hydroxides [6,7], oxyhydroxides [8,9]), sulfides [10,11], phosphides [12,13], carbides [14,15], and metal complexes [16,17], have been developed and their structure–activity relationships have been investigated. In particular, NiCo-based electrocatalysts with abundant 3d electrons and easily tunable e_g orbitals can effectively manage the covalency of metal–oxygen bonding, thereby optimizing the adsorption/desorption behavior of HMF and other intermediates, reducing the protonation/deprotonation energy barriers of active Ni sites, and significantly improving the performance of HMFOR [18]. For example, Liu et al. developed benzoyl ligand-doped $NiCo(OH)_X$ nanowires (BZ-$NiCo(OH)_X$), which have abundant electron-deficient Ni/Co sites for high-performance HMFOR [19]. Li et al. found that $NiCo_2O_4$ nanosheets with low Co/Ni ratios can provide more active sites, which are kinetically favorable for enhancing the intrinsic catalytic activity of HMFOR and the selectivity of FDCA products (98.6%) [20]. Yang et al. found that the introduction of F dopants into $NiCo_2O_4$ to form oxygen vacancies led to crystal structure expansion, increased electron density, and weakened metal–oxygen bonds, ultimately promoting HMF adsorption [21]. Liu et al. introduced Pd nanoclusters into the NiCo surface to obtain Pd/NiCo catalysts; the Pd atoms promoted the formation rate of active Ni^{3+}-O species, thereby enhancing the hybridization adsorption of Pd's d orbitals with the furan ring of HMF [22]. The above reports indicate that the current research on HMF catalysts is primarily focused on the structural and performance regulation of single NiCo-based oxides or hydroxides. However, the impact of NiCo dual-species hybrids or heterogeneous compounds on the performance and mechanism of HMFOR remains underexplored.

In this work, the partial transformation of $NiCo_2O_4$ grown on nickel foam (NF) into $NiCo(OH)_2$ was achieved via immersion in concentrated alkali solution, resulting in a heterogeneous structure with partial conversion from $NiCo_2O_4$ to $NiCo(OH)_2$. This process was confirmed to introduce a greater number of oxygen vacancies in the catalyst compared to the pristine $NiCo_2O_4$. The partial conversion of $NiCo_2O_4$‖$NiCo(OH)_2$ was verified by TEM, SEM, and XPS. Further electrochemical performance evaluations revealed that the NF@NiCo-H/O catalyst exhibited rapid HMFOR reaction kinetics, enhanced catalytic activity, stability, and superior FDCA selectivity in an alkaline electrolyte containing HMF. Raman spectroscopy of the NF@NiCo-H/O catalyst before and after the HMFOR reaction demonstrated that the resulting heterogeneous catalyst possessed a higher concentration of high-valent and HMFOR-active Ni^{3+}-O species compared to the $NiCo_2O_4$ catalyst, which is conducive to achieving high HMFOR performance.

2. Results and Discussion

2.1. Characterization of Structure

Figure 1a illustrates the synthetic scheme of the NF@$NiCo_2O_4$ and NF@NiCo-H/O catalysts. The partial substitution of oxygen atoms in $NiCo_2O_4$ with OH^- ions from a concentrated alkaline solution to form $NiCo(OH)_2$ is based on the fact that solids at the nanoscale can undergo flexible anion or cation exchange processes. Consequently, as shown in Equation (1), when metal cations in a metal oxide are in a solution with a high concentration of ligand molecules (L, i.e., OH^-), the O^{2-} ions will exchange with L to form

hydroxides. By controlling the reaction time, the heterogeneous NF@NiCo-H/O catalyst can be formed.

$$M_xO_y + OH^- \rightarrow xMOH^{(2y-1)+} + yO^{2-} \quad (1)$$

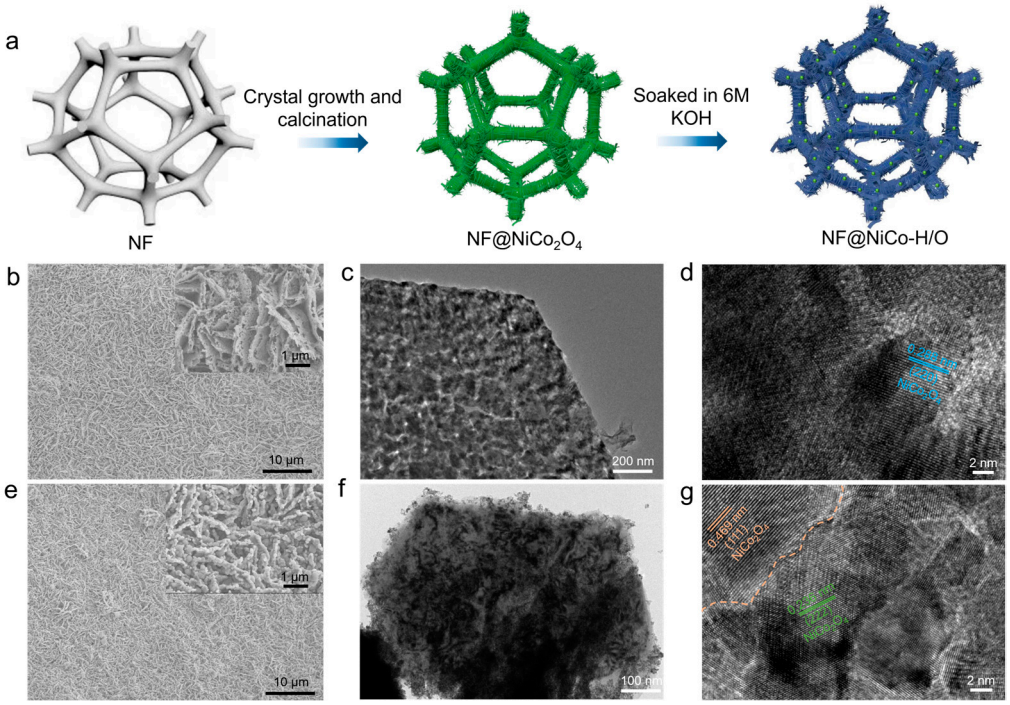

Figure 1. (**a**) Schematic illustration of the synthesis of the NF@NiCo-H/O. SEM images of the (**b**) NF@$NiCo_2O_4$ and (**e**) NF@NiCo-H/O, with insets showing the corresponding magnified images. TEM images for NF@$NiCo_2O_4$ with (**c**) low- and (**d**) high-magnification. TEM images for NF@NiCo-H/O with (**f**) low- and (**g**) high-magnification TEM.

As shown in the SEM image in Figure 1b, NF@$NiCo_2O_4$ is densely grown on the NF substrate, and the initial $NiCo_2O_4$ exhibits a 2D porous sheet morphology at the micrometer scale. This porous sheet structure is expected to expose a greater number of accessibly active sites. In sharp contrast, after the concentrated alkali reaction, the O^{2-} ions in the $NiCo_2O_4$ crystals spontaneously exchange with OH^- ions, leading to the formation of $NiCo(OH)_2$ on the surface of the $NiCo_2O_4$ crystals and ultimately resulting in the heterogeneous NF@NiCo-H/O. The SEM image in Figure 1e displays the 2D sheet morphology of NF@NiCo-H/O. Compared with NF@$NiCo_2O_4$, the surface of NF@NiCo-H/O appears rougher overall. The TEM image of NF@$NiCo_2O_4$ shown in Figure 1c reveals that the micrometer-scale NF@$NiCo_2O_4$ is composed of many small $NiCo_2O_4$ particles that are piled up, with numerous gaps between the particles, which is beneficial for the rapid mass transfer of electrolytes and other reactive substances. The high-magnification HRTEM image shows a lattice spacing of 0.288 nm, corresponding to the (220) crystal plane of $NiCo_2O_4$, indicating that the prepared NF@$NiCo_2O_4$ has a good crystalline structure (Figure 1d). In stark contrast to the formation of NF@$NiCo_2O_4$, the TEM image of NF@NiCo-H/O shows many crystals with lower contrast (Figure 1f), attributed to the formation of $NiCo(OH)_2$. In addition, many small nanoparticles are present on the surface of $NiCo(OH)_2$. The HRTEM image further indicates that these small nanoparticles are composed of $NiCo_2O_4$ with lattice spacings of 0.469 nm and 0.236 nm (Figure 1g). These characterizations demonstrate that after concentrated alkali treatment, the $NiCo_2O_4$ catalyst is partially transformed into $NiCo(OH)_2$, that is, the formation of the heterogeneous $NiCo(OH)_2||NiCo_2O_4$ catalyst.

X-ray diffraction (XRD) was employed to conduct the crystalline analysis of the synthesized catalysts. Owing to the growth of $NiCo_2O_4$ and $NiCo(OH)_2/NiCo_2O_4$ catalysts on the highly conductive NF surface, severe Ni characteristic diffraction peaks from the NF substrate were generated during the PXRD test, thereby masking the characteristic diffraction peak signals of the $NiCo_2O_4$ and $NiCo(OH)_2/NiCo_2O_4$ catalysts grown on its surface. To obtain better PXRD signals, NF@$NiCo_2O_4$ and NF@NiCo-H/O were first subjected to thorough ultrasonication in ethanol, followed by centrifugation, drying, and collection to obtain the corresponding powders. As shown in Figure 2a, a series of diffraction peaks appeared for NF@$NiCo_2O_4$ powder at 18.9°, 31.1°, 36.7°, 38.4°, 44.6°, 55.4°, 59.1°, 64.9°, 68.3°, and 77.5°, which correspond to $NiCo_2O_4$ of PDF#20-0781, indicating that $NiCo_2O_4$ was well grown on the NF surface. For the NF@NiCo-H/O, a series of $NiCo_2O_4$ diffraction peaks of PDF#20-0781 still existed, demonstrating the presence of $NiCo_2O_4$ on its surface. However, the intensity of the $NiCo_2O_4$ diffraction peaks decreased, suggesting a reduction in the amount of $NiCo_2O_4$. Moreover, a sharp peak appeared at 10.2°, corresponding to the (001) plane of $NiCo(OH)_2$, which further indicated that the decreased $NiCo_2O_4$ diffraction peak signals were due to the successful partial transformation of $NiCo_2O_4$ into $NiCo(OH)_2$.

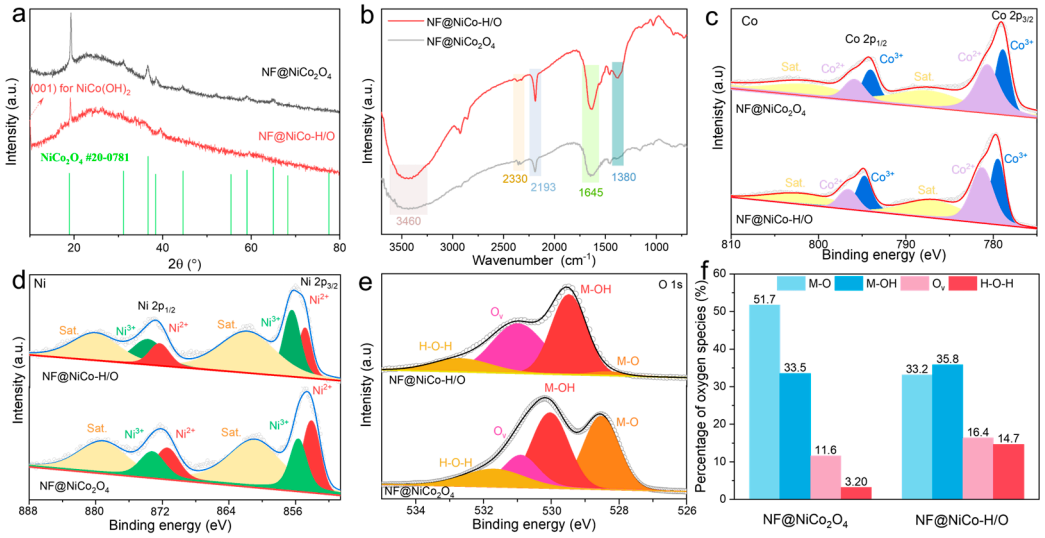

Figure 2. NF@$NiCo_2O_4$ catalyst and the NF@NiCo-H/O of (**a**) PXRD patterns, (**b**) FT-IR spectra. (**c**–**f**) XPS spectrum of (**c**) Co 2p, (**d**) Ni 2p, (**e**) O 1s, and (**f**) the proportion of different oxygen species.

As shown in Figure 2c, FT-IR spectra of NF@$NiCo_2O_4$ and NF@NiCo-H/O are revealed. The broad peaks appearing at 3250–3600 cm^{-1} are attributed to the stretching vibrations of interlayer bonded OH^- in hydroxides or O–H vibrations of surface-adsorbed water molecules [23]. The strong peak at 2330 cm^{-1} corresponds to the stretching vibrations of CO_2 in the air. The strong peak at 2193 cm^{-1} is associated with water molecules adsorbed on the catalyst surface, while the bending vibration signal of adsorbed water is observed at 1645 cm^{-1} [24]. The small peak at 1380 cm^{-1} is attributed to the bending vibration of nitrate anions intercalated in the hydroxide layers [25]. Compared with the NF@$NiCo_2O_4$, the signal intensities of the peaks at 3460, 1645, and 1380 cm^{-1} for NF@NiCo-H/O are enhanced, which, once again, confirms the successful preparation of the heterogeneous catalyst. The surface composition and elemental valence states of the catalysts were analyzed using XPS spectra. As shown in Figure 2c, both catalysts exhibit Co^{3+} (778.9 eV), Co^{2+} (780.7 eV), and corresponding satellite peaks (787.9 eV). However, NF@NiCo-H/O shows a lower Co^{3+}/Co^{2+} peak ratio (1.02) compared with the NF@$NiCo_2O_4$ (1.17), supporting the reduction of high-valent Co^{3+} species in NF@NiCo-H/O. For the metal Ni element (Figure 2d), both catalysts exhibit significant Ni^{3+} (854.1 eV), Ni^{2+} (855.7 eV), and

satellite peaks (860.9 eV). Importantly, the Ni^{3+}/Ni^{2+} peak ratio significantly increases from 0.74 ($NF@NiCo_2O_4$) to 1.26 (NF@NiCo-H/O). This decrease in the valence state of Co and increase in that of Ni indicate that partial electron transfer (PET) occurs within the NF@NiCo-H/O crystal, that is, from Co to Ni. The occurrence of this PET also promotes the formation of high-valent active Ni^{3+} species, supporting high-performance HMFOR.

2.2. Performance of HMFOR

The HMFOR and OER performance of $NF@NiCo_2O_4$ and NF@NiCo-H/O were evaluated in 1.0 M KOH electrolyte with and without 50 mM HMF using a three-electrode system. Figure 3a shows the linear sweep voltammetry (LSV) curves, with the solution without HMF serving as the control. As shown in Figure 3b, NF@NiCo-H/O required only 1.317 V, 1.395 V, and 1.443 V to achieve current densities of 20 mA cm^{-2}, 50 mA cm^{-2}, and 100 mA cm^{-2}, respectively, which are significantly lower than those of $NF@NiCo_2O_4$ (1.413 V, 1.458 V, and 1.514 V). Moreover, NF@NiCo-H/O achieved a limiting current density of 380 mA cm^{-2} at a voltage of 1.7 V, which is notably higher than that of the $NF@NiCo_2O_4$ catalyst (250 mA cm^{-2}). Compared with the OER performance in 1.0 M KOH electrolyte without 50 mM HMF, the HMFOR performance of both NF@NiCo-H/O and $NF@NiCo_2O_4$ catalysts was significantly superior to their OER performance. Specifically, the potential difference between HMFOR and OER for the NF@NiCo-H/O catalyst at 100 mA cm^{-2} was 197 mV, while for the $NF@NiCo_2O_4$ catalyst at 20 mA cm^{-2}, the HMFOR and OER potential difference was 236 mV. In addition, the NF@NiCo-H/O catalyst outperforms the recently reported non-noble metal catalysts (Figure 3f) [26–32], which also demonstrates the great potential of heterogeneous NF@NiCo-H/O catalysts for HMFOR.

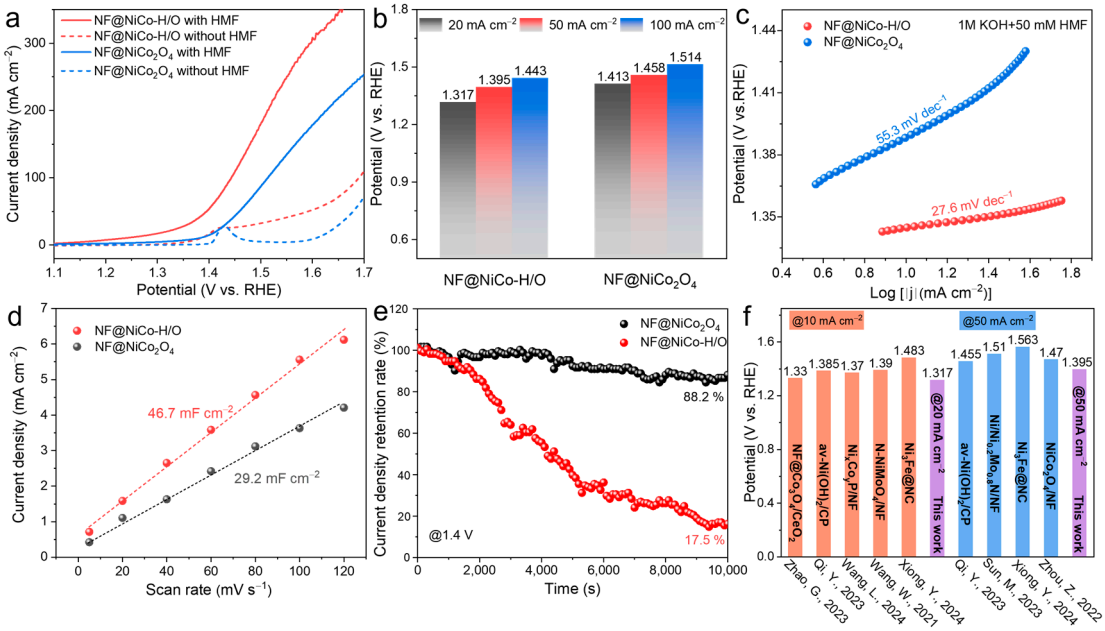

Figure 3. The $NF@NiCo_2O_4$ and NF@NiCo-H/O of (**a**) the LSV profiles, (**b**) the corresponding potentials value for current density of 20, 50, 100 mA cm^{-2}, (**c**) Tafel plot, (**d**) capacitive currents as a function of scan rates, and (**e**) chronoamperometry measurement at 1.4 V. (**f**) Comparison of HMFOR activity in this work [26–32].

The LSV curves and Tafel equation ($\eta = a + b \cdot \log j$) are employed to obtain the Tafel slope, where η represents the overpotential, j denotes the current density, and the slope b corresponds to the Tafel slope. A lower Tafel slope reflects a faster electron transfer or a more facile kinetic nature of the chemical steps in the electrocatalytic reaction. The corresponding Tafel plot in Figure 3c reveals that NF@NiCo-H/O possesses an extremely low Tafel slope

(27.6 mV dec^{-1}), which, compared with NF@$NiCo_2O_4$ (36.7 mV dec^{-1}), supports the notion that the heterogeneous NF@NiCo-H/O exhibits superior HMFOR catalytic kinetics than that of single-component $NiCo_2O_4$. Furthermore, the electrochemical active surface area (ECSA) of the as-prepared catalysts, an important parameter for assessing activity, was estimated through double-layer capacitance (C_{dl}), which was determined by the cyclic voltammetry curves with the different scan rates shown in Figure 3d. As shown in Figure 3d, NF@NiCo-H/O exhibits a higher C_{dl} value (46.7 mF cm^{-2}) than NF@$NiCo_2O_4$ (29.2 mF cm^{-2}), supporting the presence of a heterogeneous interface and a large number of high-valent Ni^{3+} species in NF@NiCo-H/O, which may be the reasons for the high ECSA. The long-term durability of the two catalysts was also investigated. During a chronoamperometry measurement at 1.4 V (in 1.0 M KOH electrolyte containing 50 mM HMF, without replacing the electrolyte during the test). After a reaction process of 10,000 s, the current density of NF@NiCo-H/O showed a decrease of 82.5% (Figure 3e). In sharp contrast, NF@$NiCo_2O_4$ exhibited only an 11.8% decrease in current. HPLC analysis of the electrolyte after the durability test revealed that the concentration of HMF in the electrolyte of NF@NiCo-H/O was essentially close to 0 mM, while that of NF@$NiCo_2O_4$ was still around 44 mM. The above durability results indicate that NF@NiCo-H/O can rapidly and continuously oxidation HMF molecules. The above results on HMFOR activity and stability suggest that the formation of a heterogeneous hybrid of $NiCo(OH)_2$ and $NiCo_2O_4$ can enhance the catalytic activity and stability of HMFOR than the single-component $NiCo_2O_4$.

The HMFOR was performed using NF@NiCo-H/O as the working electrode in an H-type electrolysis cell with an anion exchange membrane to analyze the oxidation products in detail. As shown in Figure 4a, the oxidation of HMF to FDCA typically involves two potential pathways due to the coexistence of hydroxyl and aldehyde groups [1]. For Pathway 1, the aldehyde group is preferentially oxidized to a carboxyl group to form HMFCA [2]. In Pathway 2, the hydroxyl group is oxidized to an aldehyde group to generate DFF [3]. Figure 4b,c shows that, as the reaction time progresses, the peak intensity of HMF in the HPLC spectrum decreases (15 C), while the peak intensity of FDCA increases. Meanwhile, the concentration of the product intermediate HMFCA first rises (not exceeding 1 mM) and then declines, eventually approaching zero. Additionally, a small amount of FFCA intermediate was detected, while the signal for DFF was essentially zero. Therefore, it is that this may be due to the rate of conversion of HMFCA to FFCA being slower than the rate of conversion of FFCA to FDCA, leading to the accumulation of the HMFCA intermediate until most of the HMF is consumed. This indicates that the oxidation of HMFCA to FFCA may be the rate-determining step (RDS) in the HMFOR process.

To confirm the rate-determining step in the conversion of HMF to FDCA, we investigated the oxidation rates of HMF and its intermediate products. Assuming that the oxidation process of HMF, HMFCA, and FFCA follows pseudo-first-order kinetics, the plots of $\ln(C_0/C)$ versus reaction time should be linear (Figure S3a–c). It was found that both the NF@NiCo-H/O and NF@$NiCo_2O_4$ catalysts exhibited lower rate constants for the oxidation of HMFCA compared to those for HMF and FFCA, further confirming that the conversion of HMFCA to FFCA is the RDS in both catalysts. Interestingly, the NF@NiCo-H/O catalyst showed significantly higher oxidation rates for HMF, HMFCA, and FFCA compared to NF@$NiCo_2O_4$, with rate constants that were 2.42, 2.79, and 2.86 times higher, respectively. This suggests that the reaction kinetics and RDS process of HMFOR are significantly improved through the synergistic interaction between the heterojunction phases of $NiCo_2O_4$ and $NiCo(OH)_2$. The above results indicate that the HMFOR process of NF@NiCo-H/O belongs to Pathway I, that is, HMF→HMFCA→FFCA→FDCA. Notably, NF@NiCo-H/O exhibits outstanding HMFOR performance at 1.424 V, with a high HMF conversion rate of 94.4%, an FDCA yield of 86.7%, a selectivity of 92.2%, and a Faradaic efficiency (F.E.) of

93.1%. To investigate the cyclic durability of the catalyst, twelve consecutive cycles were conducted at 1.424 V to assess the durability of the NF@NiCo-H/O catalyst. As shown in Figure 4c and Figure S4, the selectivity of FDCA, the Faradaic efficiency, and the conversion rate of HMF all remained above 85.8% after twelve cycles, demonstrating the excellent stability of the NF@NiCo-H/O.

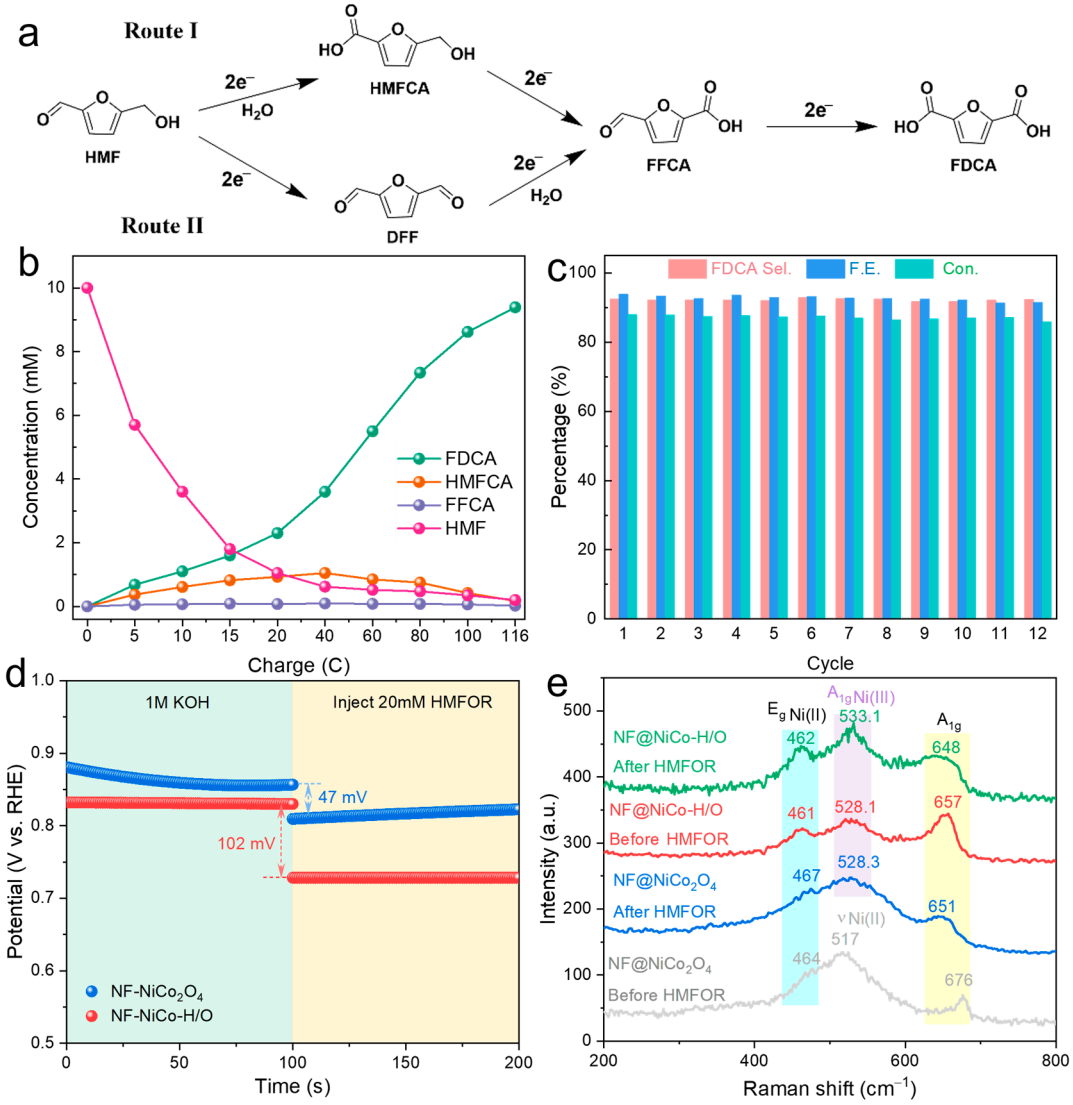

Figure 4. (**a**) Two pathways for the electrooxidation of HMF to FDCA. NF@NiCo-H/O catalyst of (**b**) concentration changes of various intermediate products under different charge quantities, (**c**) conversion rate of HMF, selectivity of FDCA, and Faradaic efficiency during twelve consecutive HMF electrooxidation reactions at 1.424 V. (**d**) OCP measurement of NF@$NiCo_2O_4$ and NF@NiCo-H/O. (**e**) Raman spectra of the NF@$NiCo_2O_4$ and NF@NiCo-H/O before and after chronoamperometry measurement.

In electrochemical reactions of biomass, the electrocatalytic activity is closely related to the concentration, accessibility of active sites, and the adsorption capacity for organic molecules [33]. During the HMFOR process, the adsorption of HMF molecules on the electrode surface plays a crucial role in constructing an efficient HMFOR. Therefore, it is of great importance to regulate the adsorption of HMF molecules. The adsorption of HMF molecules on NF@$NiCo_2O_4$ and NF@NiCo-H/O was investigated using the open-circuit potential (OCP) [4]. When 50 mM HMF was injected into a 1 M KOH solution, the OCP drop of NF@NiCo-H/O (102 mV) was larger than that of NF@$NiCo_2O_4$ (47 mV),

indicating that NF@NiCo-H/O has a stronger adsorption capacity toward HMF molecules than NF@$NiCo_2O_4$ (Figure 4d). To further explore the catalytic mechanism of NF@NiCo-H/O for HMF, Raman spectroscopy was employed to analyze the catalysts before and after the durability test. For the NF@$NiCo_2O_4$ catalyst, the Raman signals at 464, 517, and 676 cm^{-1} before the reaction correspond to the E_g (Ni^{II}-O), Ni^{II}-O, and A_{1g} vibrations of $NiCo_2O_4$ [34]. However, after the HMFOR stability test, the NF@$NiCo_2O_4$ catalyst exhibited a Raman signal at 528.3 cm^{-1}, corresponding to the A_{1g} (Ni^{III}-O) vibration of nickel-based hydroxides, and the A_{1g} vibration at 676 cm^{-1} red-shifted to 651 cm^{-1} with a decrease in intensity, indicating partial transformation of the NF@$NiCo_2O_4$ catalyst's surface, resulting in the formation of more high-valent and HMFOR-active Ni^{3+}-O species [35]. In contrast, the NF@NiCo-H/O catalyst exhibited the A_{1g} (Ni^{III}-O) vibration signal of nickel-based hydroxides before the reaction. After the HMFOR stability test, the A_{1g} (Ni^{III}-O) vibration signal of nickel-based hydroxides blue-shifted by 5 cm^{-1} and increased in intensity, while the A_{1g} vibration signal at 657 cm^{-1} decreased, further indicating that more $NiCo_2O_4$ structures were transformed into HMFOR-active nickel-based hydroxides, that is, more Ni^{3+}-O species were generated.

Furthermore, ICP-OES analysis was performed on the NF@NiCo-H/O catalysts before and after the HMFOR stability test. Notably, the Co/Ni ratio of the NF@NiCo-H/O decreased from 2.3 before testing to 1.9 after testing, indicating partial dissolution of metallic Co species and structural evolution of the catalyst. High-resolution XPS characterization was further employed to investigate the changes in valence states and electronic structures of the catalysts before and after HMFOR stability testing. The electronic structural changes of metallic Ni and Co species were analyzed by XPS spectra. The atomic percentages obtained by XPS reveal that the Ni/Co atomic ratio on the surface of the NF@NiCo-H/O catalyst has increased from 0.70 before testing to 1.16 after testing (Figure S5a). As shown in Figure S5b,d, compared to the Ni^{3+}/Ni^{2+} ratio of 1.26 in the NF@NiCo-H/O-before testing, the high-resolution Ni 2p spectra of the NF@NiCo-H/O-after testing show only the presence of Ni^{3+} species. Additionally, the high-resolution Co 2p spectra show a lower Co^{3+}/Co^{2+} ratio (0.44) for NF@NiCo-H/O-after testing compared to the value of 1.17 toward NF@NiCo-H/O-before testing (Figure S5c). Additionally, significant differences were observed in the high-resolution O 1s spectra. As shown in Figure S5e,f, the M-O bonds disappeared in the NF@NiCo-H/O-after testing, and the proportion of oxygen vacancies increased significantly. These changes in the high-resolution XPS spectra indicate that partial dissolution of metallic Co species occurred on the surface of the NF@NiCo-H/O-after testing, with some electrons from Ni being transferred to Co (inset of Figure S5d), leading to partial structural evolution on the catalyst surface, forming a heterogeneous interface $NiCo_2O_4$||$NiCo(OH)_2$ and generating more Ni^{3+}-O species and oxygen vacancies. The SEM image of the NF@NiCo-H/O-after testing also supports this (Figure S6). These findings are consistent with the Raman results presented in the revised manuscript (Figure 4e).

Previous literature has indicated that nickel/cobalt species can work synergistically to enhance the catalytic activity and stability of HMFOR [2,3]. Consequently, we delved further into the synergistic catalytic mechanism of nickel and cobalt in the NF@NiCo-H/O catalyst. To this end, we synthesized monometallic heterojunction catalysts containing only nickel or cobalt (denoted as NF@Ni-H/O and NF@Co-H/O catalysts), using the same synthesis procedure. As depicted in Figure S7a,b, the LSV curves and potential values at 10, 50, and 100 mA cm^{-2} demonstrate the following activity order: NF@NiCo-H/O > NF@$NiCo_2O_4$ > NF@Ni-H/O > NF@Co-H/O. Specifically, the NF@Ni-H/O catalyst performs markedly better than the NF@Co-H/O catalyst. Moreover, the NF@NiCo-H/O catalyst, which incorporates both nickel and cobalt, exhibits the highest catalytic activity.

Hence, in this study, it is proposed that cobalt and nickel in the NF@NiCo-H/O catalyst synergistically catalyze HMF conversion, leading to high HMFOR activity.

Previous literature has also indicated that different metal species can selectively oxidize different functional groups of HMF [8]. Thus, to analyze the role of individual Ni, Co, and bimetallic Ni/Co catalysts in the selective oxidation of HMF, we compared their cyclic voltammetry (CV) curves on 2-furaldehyde and furfuryl alcohol. As shown in Figure S8, all single-metal (Co and Ni) and bimetallic catalysts (NF@NiCo-H/O and NF@$NiCo_2O_4$) exhibited higher activity for furfuryl alcohol catalysis than for furaldehyde catalysis. At 1.4 V, the activity order for the four catalysts was NF@NiCo-H/O > NF@$NiCo_2O_4$ > NF@Ni-H/O > NF@Co-H/O, based on the current density. These results confirm that the synergistic effect between Ni/Co sites effectively accelerates the electrooxidation of both hydroxyl and aldehyde groups.

In summary, the above results indicate that the heterojunction interface formed between $NiCo_2O_4$ and $NiCo(OH)_2$, namely, $NiCo_2O_4$||$NiCo(OH)_2$, may facilitate the generation of high-activity Ni^{3+}-O species during the HMF oxidation process. In addition, through the synergistic action of cobalt and nickel metal species, the catalytic activity, selectivity, and long-term durability of the high-activity Ni^{3+}-O species towards HMF can be significantly enhanced.

3. Materials and Methods

3.1. Materials

Anhydrous ethanol (≥99.7%), acetone (≥99.5%), hydrochloric acid (36.0–38.0%), cobalt nitrate hexahydrate (99%), nickel nitrate hexahydrate (99%), urea (99%), ammonium chloride (≥99.5%), chromatographic-grade methanol, and chromatographic-grade formamide were purchased from Shanghai Guoyao Co., Ltd., Shanghai, China. 5-Hydroxymethylfurfural (95%) was obtained from Aladdin Reagents Co., Ltd., Riverside, CA, USA.

3.2. Preparation of NF@$NiCo_2O_4$

A piece of NF (2 × 0.5 cm) was subjected to ultrasonic cleaning for 15 min in a sequence of acetone, 1 M HCl, deionized water, and ethanol. The cleaned NF was then dried in an oven at 40 °C and kept for further use. Subsequently, a piece of clean NF was placed into a solution containing 2.0 mmol $Co(NO_3)_2{\cdot}6H_2O$, 1.0 mmol $Ni(NO_3)_2{\cdot}6H_2O$, 12 mmol urea, and 20 mmol ammonium chloride, which were mixed and dissolved in a mixture of 20 mL deionized water and 20 mL ethanol. This solution, along with the NF, was transferred into a 100 mL Teflon-lined stainless-steel autoclave and subjected to solvothermal reaction at 120 °C. After 2 h, the electrode was naturally cooled to room temperature and washed several times with deionized water and ethanol. The resulting electrode was heated to 300 °C at a heating rate of 5 °C·min^{-1} and maintained at this temperature for 2 h to obtain the NF@$NiCo_2O_4$.

3.3. Preparation of NF@NiCo-H/O

A piece of NF@$NiCo_2O_4$ was immersed in a 6 M KOH solution and stirred slowly for 12 h. The catalyst was then taken out and washed several times with deionized water and ethanol to obtain the NF@NiCo-H/O.

3.4. Physicochemical Characterization

The crystalline structure of the catalysts was determined using an X-ray diffractometer (XRD, Philips X-Pert Pro, Almere, The Netherlands) with Cu Kα radiation (1.5418 Å). The microscopic structure were analyzed by transmission electron microscopy (TEM, Tecnai G2

F20, Hillsboro, OR, USA, and JEM-2100, Tokyo, Japan) at 200 kV, in which the catalyst was first subjected to ultrasonication in an ethanol solution for 1 h, after which the catalyst was drop-cast onto a copper grid with an ultrathin carbon film. The morphology and structure of the catalyst were analyzed by Scanning electron microscopy (SEM, Hitachi SU8000, Tokyo, Japan) at 10 kV. The elemental composition and valence state were determined by X-ray photoelectron spectroscopy (XPS, ESCALAB 250Xi, Waltham, MA, USA) with a monochromatized Al Kα X-ray excitation source (1487 eV). ICP-OES was carried out on a NexION 2000-(A-10) (Waltham, MA, USA) to determine the Ni and Co concentrations. The surface structure and functional group information of the catalysts were identified using an Xplora confocal microprobe Raman system (HORIBA Jobin Yvon, Glasgow, UK) at 532 nm and Fourier-transform infrared spectroscopy (FT-IR, Nicolet Nexus, Shanghai, China).

3.5. Electrochemical Testing

Electrochemical tests were conducted using a dual potentiostat (Wuhan KEST CS2350M). The electrodes prepared as described above, a mercury oxide electrode and a carbon rod, were employed as the working electrode, reference electrode, and counter electrode, respectively. The exposed surface area of the working electrode toward as-prepared electrode is 0.5 cm^2 during the measurements. The OER or HMFOR performance was evaluated in 1 M KOH electrolyte with or without 50 mM HMF at room temperature. The catalyst was activated at a scan rate of 50 $mV \cdot s^{-1}$ until the curves overlapped in 1 M KOH with 50 mM HMF, after which other electrochemical performance tests could be carried out. The tested potentials were converted to potentials relative to the reversible hydrogen electrode (vs. RHE) through calculation. The electrochemical data were presented with 85% iR correction.

In order to quantitatively analyze the products of HMF oxidation and calculate the corresponding Faradaic efficiency, 10 μL of the electrolyte was extracted after electrolysis at a potential of 1.45 V (in a three-electrode configuration) for different amounts of charge (5C, 10C, 15C, 20C, 40C, 60C, 80C, 100C, 116C), and then neutralized with dilute sulfuric acid to neutrality. The as-solution were tested using high-performance liquid chromatography (HPLC, Waters 1525): the analysis was performed with a UV-visible detector at a detection wavelength of 265 nm; a C18 column (4.6 mm × 150 mm, Shim-pack GWS, 5 μm) was employed with mobile phase A (methanol) and B (5 mM ammonium formate aqueous solution, A:B = 3:7) at a flow rate of 0.6 $mL \cdot min^{-1}$.

The external standard method was employed for qualitative and quantitative analysis of production (HMF/FDCA/HMFCA/FFCA). HMF conversion, FDCA yield, and FE value of FDCA were calculated using the following equations:

$$\text{HMF coversion} = \frac{mole\ of\ consumed\ HMF}{mole\ of\ initial\ HMF} \times 100\% \quad (2)$$

$$\text{FDCA yield} = \frac{mole\ of\ FDCA\ formed}{mole\ of\ initial\ HMF} \times 100\% \quad (3)$$

$$\text{FE of FDCA} = \frac{mole\ of\ FDCA\ formed}{total\ charge\ passed/(6 \times F)} \times 100\% \quad (4)$$

where F is the Faraday constant (96,485 C mol^{-1}).

4. Conclusions

In summary, the partial transformation of $NiCo_2O_4$ into $NiCo(OH)_2$ was achieved via immersion in concentrated alkali solution, resulting in the formation of the heterogeneous NF@NiCo-H/O catalyst. A variety of physicochemical characterizations supported the

growth of $NiCo(OH)_2$ sub-nanoparticles on the porous micrometer-scale $NiCo_2O_4$ surface, creating abundant heterogeneous interfaces of $NiCo_2O_4$||$NiCo(OH)_2$. The HMFOR performance revealed that, compared with single-component NF@$NiCo_2O_4$, the heterogeneous NF@NiCo-H/O catalyst exhibited higher HMFOR activity and stability, as well as high HMF conversion rate (86.0%), FDCA yield (83.1%), and Faradaic efficiency (85.7%). More importantly, Raman spectra before and after the stability test indicated that the generation of more high-activity Ni^{3+}-O species on the NF@NiCo-H/O catalyst, compared with the single-component NF@$NiCo_2O_4$, during the HMFOR process, is the main reason for the higher activity and selectivity of HMFOR.

Supplementary Materials: The following supporting information can be downloaded at: https://www.mdpi.com/article/10.3390/inorganics13070211/s1, Figure S1: SEM images of low-magnification of (a) NF@$NiCo_2O_4$, and (b) NF@NiCo-H/O, and high-magnification of (c) NF@$NiCo_2O_4$, and (d) NF@NiCo-H/O; Figure S2: CV curves of (a) NF@NiCo-H/O, (b) NF@$NiCo_2O_4$ acquired at scan rates of 10, 20, 40, 60, 80, 100, and 120 mV s^{-1}; Figure S3: ln(C_0/C) based on (a) HMF, (b) HMFCA, and (c) FFCA vs the reaction time for the HMFOR process; Figure S4: CV curve of (a) NF@NiCo-H/O, (c) NF@$NiCo_2O_4$, (e) NF@Ni-H/O, and (g) NF@Co-H/O in 1 M KOH and 10 mM 2-furaldehyde solution at a scan rate of 5 mV s^{-1}. CV curve of (b) NF@NiCo-H/O, (d) NF@$NiCo_2O_4$, (f) NF@Ni-H/O, and (h) NF@Co-H/O in 1 M KOH and 10 mM furfuryl alcohol solution at a scan rate of 5 mV s^{-1}; Figure S5: XPS characterization of NF@NiCo-H/O catalysts before and after HMFOR stability testing in 1 M KOH + 50 mM HMF for 12 h. (a) The atomic ratios of the NF@NiCo-H/O catalyst before and after the HMFOR stability testing. High-resolution XPS spectra of (b) Ni 2p and (c) Co 2p, (d) the ratio of different oxidation state species of metals, (e) O 1s, and (f) proportion of different oxygen species for NF@NiCo-H/O before and after HMFOR stability testing. Inset of (d) is schematic diagram of partial electron transfer between Ni-O and Co-O; Figure S6: SEM images of the catalyst at different magnifications after HMFOR stability testing in 1 M KOH + 50mM HMF for 12 h; Figure S7: Catalysts of (a) LSV profiles in solution of 1M KOH with 50mM HMF, (b) the corresponding potentials value for current density of 10, 50, 100 mA cm^{-2}. Catalysts of (c) LSV profiles in solution of 1M KOH without 50mM HMF; Figure S8: CV curve of (a) NF@NiCo-H/O, (c) NF@$NiCo_2O_4$, (e) NF@Ni-H/O, and (g) NF@Co-H/O in 1 M KOH and 10 mM 2-furaldehyde solution at a scan rate of 5 mV s^{-1}. CV curve of (b) NF@NiCo-H/O, (d) NF@$NiCo_2O_4$, (f) NF@Ni-H/O, and (h) NF@Co-H/O in 1 M KOH and 10 mM furfuryl alcohol solution at a scan rate of 5 mV s^{-1}; Table S1: Comparison of HMFOR activity between NF@NiCo-H/L catalyst and other well-developed electrocatalysts. References [26–32] are cited in the supplementary materials.

Author Contributions: Conceptualization, Y.W.; methodology, Y.W.; software, D.Y. and W.L. (Wen Li); validation, W.L. (Wen Li), Y.L. and D.Y.; formal analysis, D.Y.; investigation, W.L. (Wanxin Liu), W.L. (Wen Li) and Y.L.; resources, Y.W.; data curation, Y.L.; writing—original draft preparation, W.L. (Wen Li) and D.Y.; writing—review and editing, W.L. (Wen Li) and Y.W.; visualization, W.L. (Wanxin Liu); supervision, Y.W.; project administration, Y.W.; funding acquisition, Y.W., W.L. (Wanxin Liu) and D.Y. contributed equally to this work; all authors analyzed the data; all authors discussed the results of this paper. All authors have read and agreed to the published version of the manuscript.

Funding: This research was supported by the Academic College Student Innovation and Entrepreneurship Training Program (No. S202210546010), the National Natural Science Foundation Program of China (No. 52301271), and the Natural Science Foundation of Hunan Province of China (No. 2024JJ6087).

Institutional Review Board Statement: Not applicable.

Informed Consent Statement: Not applicable.

Data Availability Statement: The raw data supporting the conclusions of this article will be made available by the authors upon request.

Conflicts of Interest: The authors declare no conflicts of interest.

References

1. Wu, X.; Wang, Y.; Wu, Z.-S. Design principle of electrocatalysts for the electrooxidation of organics. *Chem* **2022**, *8*, 2594–2629. [CrossRef]
2. Chen, C.; Lv, M.; Hu, H.; Huai, L.; Zhu, B.; Fan, S.; Wang, Q.; Zhang, J. 5-Hydroxymethylfurfural and its downstream chemicals: A review of catalytic routes. *Adv. Mater.* **2024**, *36*, 2311464.
3. Simoska, O.; Rhodes, Z.; Weliwatte, S.; Cabrera-Pardo, J.R.; Gaffney, E.M.; Lim, K.; Minteer, S.D. Advances in electrochemical modification strategies of 5-hydroxymethylfurfural. *ChemSusChem* **2021**, *14*, 1674–1686.
4. Pham, M.T.H.; Ang, A.W.Y.; Vo, T.G.; Hayashi, T.; Chiang, C.Y. Unlocking the potential of mixed-valence silver oxide for electrochemical valorization of 5-hydroxymethylfurfural into valuable products. *Mater. Today Sustain.* **2024**, *28*, 100992. [CrossRef]
5. Kubota, S.R.; Choi, K.S. Electrochemical oxidation of 5-hydroxymethylfurfural to 2, 5-furandicarboxylic acid (FDCA) in acidic media enabling spontaneous FDCA separation. *ChemSusChem* **2018**, *11*, 2138–2145. [CrossRef] [PubMed]
6. Zubair, M.; Usov, P.M.; Ohtsu, H.; Yuwono, J.A.; Gerke, C.S.; Foley, G.D.; Hackbarth, H.; Webster, R.F.; Yang, Y.; Lie, W.H.; et al. Vacancy mediated electrooxidation of 5-hydroxymethyl furfuryl using defect engineered layered double hydroxide electrocatalysts. *Adv. Energy Mater.* **2024**, *14*, 2400676. [CrossRef]
7. Woo, J.; Moon, B.C.; Lee, U.; Oh, H.S.; Chae, K.H.; Jun, Y.; Lee, D.K. Collaborative electrochemical oxidation of the alcohol and aldehyde groups of 5-hydroxymethylfurfural by NiOOH and $Cu(OH)_2$ for superior 2, 5-furandicarboxylic acid production. *ACS Catal.* **2022**, *12*, 4078–4091. [CrossRef]
8. Taitt, B.; Nam, D.; Choi, K. A comparative study of nickel, cobalt, and iron oxyhydroxide anodes for the electrochemical oxidation of 5-hydroxymethylfurfural to 2, 5-furandicarboxylic acid. *ACS Catal.* **2018**, *9*, 660–670. [CrossRef]
9. Bender, M.T.; Choi, K.S. Electrochemical oxidation of HMF via hydrogen atom transfer and hydride transfer on NiOOH and the impact of NiOOH composition. *ChemSusChem* **2022**, *15*, e202200675. [CrossRef]
10. Han, W.; Tang, M.; Li, J.; Li, X.; Wang, J.; Zhou, L.; Yang, Y.; Wang, Y.; Ge, H. Selective hydrogenolysis of 5-hydroxymethylfurfural to 2,5-dimethylfuran catalyzed by ordered mesoporous alumina supported nickel-molybdenum sulfide catalysts. *Appl. Catal. B* **2020**, *268*, 118748. [CrossRef]
11. Sun, Y.; Wang, J.; Qi, Y.; Li, W.; Wang, C. Efficient electrooxidation of 5-hydroxymethylfurfural using Co-doped Ni_3S_2 catalyst: Promising for H_2 production under industrial-level current density. *Adv. Sci.* **2022**, *9*, 2200957.
12. Xu, X.; Song, X.; Liu, X.; Wang, H.; Hu, Y.; Xia, J.; Chen, J.; Shakouri, M.; Guo, Y.; Wang, Y. A highly efficient nickel phosphate electrocatalyst for the oxidation of 5-hydroxymethylfurfural to 2,5-furandicarboxylic acid. *ACS Sustain. Chem. Eng.* **2022**, *10*, 5538–5547. [CrossRef]
13. Fu, J.; Yang, G.; Jiao, Y.; Tian, C.; Yan, H.; Fu, H. Ni-Cu-based phosphide heterojunction for 5-hydroxymethylfurfural electrooxidation-assisted hydrogen production at large current density. *Nano Energy* **2024**, *127*, 109727.
14. Huang, R.; Jiang, J.; Liang, J.; Wang, S.; Chen, Y.; Zeng, X.; Wang, K. Selective hydrogenation of 5-hydroxymethylfurfural triggered by a high Lewis acidic Ni-based transition metal carbide catalyst. *Green Energy Environ.* **2025**, *10*, 573–584. [CrossRef]
15. Li, Y.; Alorku, K.; Shen, C.; Yan, L.; Li, Q.; Tian, X.; Li, W.; Xu, Y.; Wang, C.; Li, C.; et al. In-situ redispersion of Ni@C catalyst boosts 5-hydroxymethylfurfural electrooxidation by increasing Ni^{4+} sites. *Appl. Catal. B* **2024**, *357*, 124250.
16. Huang, N.; Chu, B.; Chen, D.; Shao, B.; Zheng, Y.; Li, L.; Xiao, X.; Xu, Q. Rational design of a quasi-metal–organic framework by ligand engineering for efficient biomass upgrading. *J. Am. Chem. Soc.* **2025**, *147*, 8832–8840. [CrossRef]
17. Yang, S.; Guo, Y.; Zhao, P.; Jiang, H.; Shen, H.; Chen, Z.; Jiang, L.; Xue, X.; Zhang, Q.; Zhang, H. Unraveling the electrooxidation mechanism of 5-(hydroxymethyl)furfural at a molecular level via nickel-based two-dimensional metal–organic frameworks catalysts. *ACS Catal.* **2024**, *14*, 449–462. [CrossRef]
18. Prabhu, P.; Wan, Y.; Lee, J.M. Electrochemical conversion of biomass derived products into high-value chemicals. *Matter* **2020**, *3*, 1162–1177. [CrossRef]
19. Liu, X.; Wang, X.; Mao, C.; Qiu, J.; Wang, R.; Liu, Y.; Chen, Y.; Wang, D. Ligand-hybridization activates lattice-hydroxyl-groups of $NiCo(OH)_x$ nanowires for efficient electrosynthesis. *Angew. Chem. Int. Ed.* **2024**, *63*, e202408109. [CrossRef]
20. Li, K.; Lu, H.; Shi, H. Engineering the morphology and electronic structure of $NiCo_2O_4$ to boost the electrocatalytic oxidation of 5-hydroxymethylfurfural. *ChemSusChem* **2025**, *18*, e202402605. [CrossRef]
21. Yang, S.; Xiang, X.; He, Z.; Zhong, W.; Jia, C.; Gong, Z.; Zhang, N.; Zhao, S.; Ya, C. Anionic defects engineering of $NiCo_2O_4$ for 5-hydroxymethylfurfural electrooxidation. *Chem. Eng. J.* **2023**, *457*, 141344. [CrossRef]
22. Liu, G.; Nie, T.; Song, Z.; Sun, X.; Shen, T.; Bai, S.; Zheng, L.; Song, Y. Pd Loaded NiCo hydroxides for biomass electrooxidation: Understanding the synergistic effect of proton deintercalation and adsorption kinetics. *Angew. Chem. Int. Ed.* **2023**, *135*, e202311696. [CrossRef]
23. Jadhav, H.; Roy, A.; Desalegan, B.; Seo, J. An advanced and highly efficient Ce assisted NiFe-LDH electrocatalyst for overall water splitting. *Sustain. Energy Fuels* **2020**, *4*, 312–323. [CrossRef]

24. Nagappan, S.; Karmakar, A.; Madhu, R.; Sankar, S.; Kumaravel, S.; Bera, K.; Dhandapani, H.; Sarkar, D.; Yusuf, S.M.; Kundu, S. 2D CoFe-LDH nanosheet-incorporated 1D microfibers as a high-performance OER electrocatalyst in neutral and alkaline media. *ACS Appl. Energy Mater.* **2022**, *5*, 11483–11497. [CrossRef]
25. Nyongombe, G.E.; Kabongo, G.L.; Noto, L.L.; Dhlamini, M.S. Up-scalable synthesis of highly crystalline electroactive Ni-Co LDH nanosheets for supercapacitor applications. *Int. J. Electrochem. Sci.* **2020**, *15*, 4494–4502. [CrossRef]
26. Zhao, G.; Hai, G.; Zhou, P.; Liu, Z.; Zhang, Y.; Peng, B.; Xia, W.; Huang, X.; Wang, G. Electrochemical oxidation of 5-hydroxymethylfurfural on CeO_2-modified Co_3O_4 with regulated intermediate adsorption and promoted charge transfer. *Adv. Funct. Mater.* **2023**, *33*, 2213170. [CrossRef]
27. Qi, Y.F.; Wang, K.Y.; Zhou, Y.; Sun, Y.; Wang, C. Effects of different vacancies in nickel hydroxides on the electrooxidation towards 5-hydroxymethylfurfural. *Chem. Eng. J.* **2023**, *477*, 146917. [CrossRef]
28. Wang, L.; Wang, Z.; Chu, L.; Huang, Z.; Yang, M.; Wang, G. Electronic structure modulation and morphological engineering of trifunctional Ni_xCo_yP electrode for ultrastable overall water splitting at 1 A cm^{-2} and efficient biomass oxidation valorization. *Int. J. Hydrogen Energy* **2024**, *64*, 830–841. [CrossRef]
29. Wang, W.; Wang, M. Nitrogen modulated $NiMoO_4$ with enhanced activity for the electrochemical oxidation of 5-hydroxymethylfurfural to 2, 5-furandicarboxylic acid. *Catal. Sci. Technol.* **2021**, *11*, 7326–7330. [CrossRef]
30. Xiong, Y.; Hu, S.; Jiang, J.; Liu, Y.; Zhao, W.; Ji, X.; Chen, C.; Fan, M.; Wang, K. Enhancing Ni oxidation reconstruction in Ni_3Fe nanoalloy for efficient electro-oxidation of 5-Hydroxymethylfurfural. *Chem. Eng. J.* **2024**, *499*, 156320. [CrossRef]
31. Sun, M.; Yang, J.; Huang, J.; Wang, Y.; Liu, X.; Qi, Y.; Zhang, L. Interfacial engineering of $Ni/Ni_{0.2}Mo_{0.8}N$ heterostructured nanorods realizes efficient 5-hydroxymethylfurfural electrooxidation and hydrogen evolution. *Langmuir* **2023**, *39*, 3762–3769. [CrossRef] [PubMed]
32. Zhou, Z.; Xie, Y.; Sun, L.; Wang, Z.; Wang, W.; Jiang, L.; Tao, X.; Li, L.; Li, X.; Zhao, G. Strain-induced in situ formation of NiOOH species on CoCo bond for selective electrooxidation of 5-hydroxymethylfurfural and efficient hydrogen production. *Appl. Catal. B* **2022**, *305*, 121072. [CrossRef]
33. Ghosh, S.; Bagchi, D.; Mondal, I.; Sontheimer, T.; Jagadeesh, R.; Menezes, P. Deciphering the role of nickel in electrochemical organic oxidation reactions. *Adv. Energy Mater.* **2024**, *14*, 2400696. [CrossRef]
34. Iliev, M.N.; Silwal, P.; Loukya, B.; Datta, R.; Kim, D.H.; Todorov, N.D.; Pachauri, N.; Gupta, A. Raman studies of cation distribution and thermal stability of epitaxial spinel $NiCo_2O_4$ films. *J. Appl. Phy.* **2013**, *114*, 033514. [CrossRef]
35. Wu, Y.J.; Yang, J.; Tu, T.X.; Li, W.Q.; Zhang, P.F.; Zhou, Y.; Li, J.F.; Li, J.T.; Sun, S.G. Evolution of cationic vacancy defects: A motif for surface restructuration of OER precatalyst. *Angew. Chem. Int. Ed.* **2021**, *60*, 26829–26836. [CrossRef]

Disclaimer/Publisher's Note: The statements, opinions and data contained in all publications are solely those of the individual author(s) and contributor(s) and not of MDPI and/or the editor(s). MDPI and/or the editor(s) disclaim responsibility for any injury to people or property resulting from any ideas, methods, instructions or products referred to in the content.